DENTAL MATERIALS 35 (2019) 257–269

Available online at www.sciencedirect.com

ScienceDirect

journal homepage: www.intl.elsevierhealth.com/journals/dema

Residual strain mapping through pair distribution function analysis of the porcelain veneer within a yttria partially stabilised zirconia dental prosthesis

Alexander J.G. Lunt[a,*,1], *Philip Chater*[b], *Annette Kleppe*[b], *Nikolaos Baimpas*[a,2], *Tee K. Neo*[c], *Alexander M. Korsunsky*[a]

[a] *Department of Engineering Science, University of Oxford, Parks Road, Oxford, OX1 3PJ, United Kingdom*
[b] *Diamond Light Source, Harwell Science and Innovation Campus, Didcot, OX11 0QX, United Kingdom*
[c] *Specialist Dental Group, Mount Elizabeth Orchard, #08-03/08-08/08-10, 228510, Singapore*

ARTICLE INFO

Article history:
Received 9 July 2018
Received in revised form
31 October 2018
Accepted 14 November 2018

Keywords:
Dental porcelain
Yttria partially stabilised zirconia
Pair distribution function analysis
Synchrotron X-ray diffraction
Residual strain
Ring-core
Focused ion beam milling
Digital image correlation

ABSTRACT

Objective. Residually strained porcelain is influential in the early onset of failure in Yttria Partially Stabilised Zirconia (YPSZ) – porcelain dental prosthesis. In order to improve current understanding it is necessary to increase the spatial resolution of residual strain analysis in these veneers.

Methods. Few techniques exist which can resolve residual stress in amorphous materials at the microscale resolution required. For this reason, recent developments in Pair Distribution Function (PDF) analysis of X-ray diffraction data of dental porcelain have been exploited. This approach has facilitated high-resolution (70 μm) quantification of residual strain in a YPSZ-porcelain dental prosthesis.

In order to cross-validate this technique, the sequential ring-core focused ion beam and digital image correlation approach was implemented at a step size of 50 μm. This semi-destructive technique exploits microscale strain relief to provide quantitative estimates of the near-surface residual strain.

Results. The two techniques were found to show highly comparable results. The residual strain within the veneer was found to be primarily tensile, with the highest magnitude stresses located at the YPSZ-porcelain interface where failure is known to originate. Oscillatory tensile and compressive stresses were also found in a direction parallel to the interface, likely to be induced by the multiple layering used during fabrication.

Significance. This study provides the insights required to improve prosthesis modelling, to develop new processing routes that minimise residual stress and ultimately to reduce prosthesis failure rates. The PDF approach also offers a powerful new technique for microscale strain quantification in amorphous materials.

Abbreviations: DIC, Digital image correlation; FE, Finite element; FIB, Focused ion beam; LRO, Long rangeorder; MBLEM, Multi beam laboratory for engineering microscopy; MRO, Medium range order; PDF, Pair distribution function; SEM, Scanning electron microscopy; SRO, Short range order; XRD, X-ray diffraction; YPSZ, Yttria partially stabilised zirconia.

* *Corresponding author.*
E-mail address: alexander.lunt@cern.ch (A.J.G. Lunt).
[1] Present address: CERN, CH-1211, Geneva 23, Switzerland.
[2] Present address: Atkins Ltd, London Rd, Derby DE24 8UP, UK.

https://doi.org/10.1016/j.dental.2018.11.013
0109-5641/

1. Introduction

In recent decades the high strength, high toughness, excellent biocompatibility and appealing aesthetics of Yttria Partially Stabilised Zirconia (YPSZ) has ensured that this ceramic has become the restorative material of choice used in premium dental prostheses [1]. During the manufacture of these copings, YPSZ is coated with a porcelain veneer in order to match the shade and pearlescence of the patients' existing teeth and to reduce wear during occlusal contact [2]. However, along with these benefits this manufacturing approach is known to induce the primary failure mode of these prostheses: near interface chipping of the porcelain veneer [3].

Recent studies into the origin of this behaviour have suggested that failure arises from modifications to the microstructure (and mechanical behaviour) of porcelain within the first few microns of the interface [4–7]. Although elemental diffusion is known to influence this weakened near interface region, the primary driving force behind many of these mechanical changes is the tensile residual stress (or strain) which is generated during manufacture [8–10]. These stresses are induced by a combination of thermal expansion mismatch between porcelain and YPSZ [11], the tetragonal to monoclinic phase transformation of YPSZ [12] and the multiple layer approach used to produce the prosthesis veneer [13]. The low tensile fracture toughness of porcelain means that these stresses, in combination with mastication loads, are sufficient to induce tensile failure of the near-interface veneer [14]. To reduce the likelihood of failure, an improved understanding of the residual strain state within the porcelain is crucial.

A number of microscale semi-destructive residual stress and strain analysis techniques have previously been applied to dental prosthesis cross sections both within YPSZ and porcelain. Spatially resolved nanoindentation testing has previously shown that porcelain is on average in a state of tension, and that a variation in the residual stress state corresponding to the veneer layering process can be detected [11,15]. Recent developments of the ring-core Focused Ion Beam (FIB) milling and Digital Image Correlation (DIC) technique have resulted in higher resolution (micro-scale) and more precise residual stress analysis [16] in comparison to the methods successfully applied previously to measure the average strain within a veneer [17]. The ~0.5 mm step size used in this study was insufficient to capture the variations in residual stress induced by the multi-layered manufacturing approach. However, both tensile and compressive stresses were observed, suggesting that the approach would be capable of resolving the strain response at higher resolution.

In the past few decades, micro-focused synchrotron X-ray diffraction has become well established as one of the most suitable techniques for microscale structural analysis and residual strain quantification [18]. The regularly spaced structure of atomic planes within crystalline materials produces sharp X-ray diffraction reflexes which forms a convenient and precise basis for the XRD lattice strain quantification approach [19,20]. Amorphous materials such as porcelain produce diffraction patterns with broad and diffuse peaks which, despite containing large amounts of structural information, cannot be analysed for strain in the same manner [21]. In order to extract local structure information, diffraction data collected over a sufficient momentum transfer range can, after careful correction and background subtraction, be Fourier transformed to give the Pair Distribution Function (PDF) [22]. These representations of the probability of finding an atom at a particular interatomic radial distance characterise the average distribution of atoms within the amorphous material. Strain causes changes in the arrangements of atoms within the material, which is reflected in changes in the peak centre positions (shifts) within the PDF [23,24]. For amorphous materials subjected to elastic deformation, a linear correlation between the macroscopic strain and PDF peak centre position has been reported [25].

In a recent experimental and modelling study, the influence of macroscopic strain on the PDF pattern of dental porcelain was considered in detail. In situ loading in the 4-point bending configuration was used to impose a well-characterised strain distribution within porcelain, and the impact on the resulting PDF-derived strain distributions was assessed. As well as providing insight into the fundamental atomic scale response of porcelain, critically the relationships between PDF peak shift and macroscopic strain were revealed by this investigation. These results enable the quantification of residual strain within the sample of interest by the combination of X-ray scattering and PDF analysis. In the present study, this approach is used to perform residual strain profiling within a porcelain dental veneer of YPSZ copings.

In order to validate this new technique, the recently developed sequential spatially resolved ring-core FIB milling and DIC approach has been applied at the same location [27]. This analysis has been performed at a step size of 50 μm (i.e. an order of magnitude finer than the 0.5 mm step previously implemented) to capture the variation of strain over multiple veneering layers. Strain evaluation was performed in directions parallel and perpendicular to the interface that correspond to the two key distinct orientations within the system [28]. DIC marker outlier removal was also implemented in this study to increase the reliability and precision of the results with respect to those presented previously [29].

2. Materials and methods

2.1. *Sample preparation*

The incisal dental prosthesis examined in this study was manufactured by the Specialist Dental Group, Singapore, using the manufacturing routes prescribed by the suppliers. Wieland Dental Zenotec Zr Bridge [30] YPSZ was used to make the coping base and Ivoclar Vivadent IPS e.max Ceram [31] porcelain was veneered onto this in a multiple stage process at a firing temperature of 730 °C and holding time of 2 min. The coefficient of thermal expansion of the Zr Bridge is slightly larger ($10.5 \times 10^{-6} K^{-1}$) than that of the IPS e.max Ceram ($9.5 \times 10^{-6} K^{-1}$) such that the thermal expansion mismatch generates a low magnitude tensile stress within the YPSZ and a compressive stress within the porcelain veneer. The completed prosthesis was mounted in epoxy and sectioned in a such a way that at the location of interest the YPSZ-porcelain

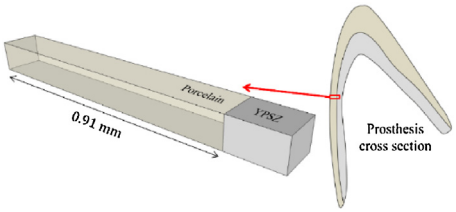

Fig. 1 – Prosthesis cross section showing the location of line scan and the relative orientation of interface between YPSZ and porcelain.

interface was perpendicular to the cross-section surface, as shown in Fig. 1. The thickness of the prosthesis slice was selected to be 2 mm in order to maximise the diffracted signal during the synchrotron X-ray scattering experiment.

In order to minimise the residual stresses induced during sample preparation, a Buehler Isomet Diamond Saw was used to perform gentle sectioning. It should be noted that the sectioning using this approach can have a localised impact on the surface residual stress and strength of ceramics [32]. Therefore, it is important to estimate the size of the impact zone, which can be predicted through knowledge of the grinding medium and Hertzian contact theory [33]. The resulting expressions reveal that the size of the nominally influenced region is expected to be less than three times the diameter of the grit size. In this study, a diamond blade with a grit size of 60 μm was used to section the sample and therefore a 250 μm layer was removed from the two cut surfaces. This process was performed using progressively refined grinding and diamond polishing, in which the same considerations of Hertzian contact theory and grinding medium size were used to produce a surface in which the size of the influenced zone had been minimised to less than 300 nm.

In the case of the PDF analysis, this influence of the impacted zone will be averaged through the entire 2 mm cross section. This represents 0.03% of the gauge volume and will therefore have a minimal impact on the result. For the ring-core analysis, this region represents a maximum of 6% of the gauge volume. However, it should be noted that this represents an overestimate and that the stress measurements are being performed within the surface plane of the sample, and not the plane normal, which is the direction most influenced by Hertzian contact [33].

Consideration of the impact of relief intrinsically induced by the sectioning process must also be performed in order to determine the difference between the stress state originally present and that measured after sectioning. This concept has previously been the focus of numerous discussions in the literature [34,35], in which it has been shown that a good approximation to the change in the strain state is given by the square of Poisson's ratio. This means that the prosthesis cross section is a good representation for the undisturbed strain distribution with a maximum difference of ≈4% [35].

Porcelain veneers such as IPS e.max Ceram are supplied as powders that are then applied as aqueous slurry and fired to build up millimetre thick multiple layer veneers. This approach differs to that used for the monolithic Cerec 2 VITABLOC® Mark II ceramic blanks [36] examined in the study by Lunt et al. [37], however the elemental composition of the two materials are similar [36,38], with both porcelains being primarily composed of silica with reduced concentrations of other oxides. The diffraction of the two material types is therefore expected to be sufficiently similar as to facilitate an effective comparison between the results from the two materials, particularly at small atomic distances as outlined in Section 2.2.4. The effectiveness of this comparison was further confirmed by performing cross-validation of the results with those obtained by an independent method as outlined in Section 3.

2.2. PDF analysis

2.2.1. X-ray diffraction

The X-ray diffraction approach implemented in this study builds and expands the approach by Lunt et al. [37]. An X-ray energy of 76 keV and circularly collimated beam cross section of 70 μm was used to perform transmission diffraction at beamline I15 at Diamond Light Source, UK. In order collect data at a high momentum transfer ($Q_{max} = 25.1 Å^{-1}$) a Perkin Elmer flat panel 1621 EN area was placed 262 mm downstream from the sample. For this experiment, the sample-to-detector distance calibration was performed using lanthanum hexaboride (LaB_6, NIST SRM 660b) [37].

An optical microscope was used to align the sample region of interest with the incident beam and translation stages were used to move the sample to position different regions within the sample into the beam. The data collection routine, as previously performed by Lunt et al. [37], consisted of a one minute dark field data collection (D_R) (in absence of X-rays), followed by a one minute raw collection exposure (R); this sequence was repeated 12 times at each point on the sample. Flat field data collection was also performed by removing the sample and repeating the stage movements and image collections previously performed during the data acquisition (F). Dark field correction in the absence of X-rays was also performed during the flat field collection routine (D_F). The resulting corrected image (C) at each collection point was therefore given by

$$C = \frac{(R - D_R) \times m}{F - D_F}, \quad (1)$$

where m is the average value of the image $F - D_F$.

X-ray scattering data were collected across the porcelain veneer of the 2 mm prosthesis cross section at the location shown in Fig. 1. The position of the line scan was selected to be within a region where the YPSZ-porcelain interface was uniform in the through-beam direction and to be far from the boundaries of the prosthesis; this was to reduce the impact of curvature and surface relief effects in these areas. A line scan was then performed from the YPSZ-porcelain interface to the edge of the veneer in increments of 70 μm. Thirteen points, covering a total distance of 0.91 mm, were successfully collected from within this region. The full veneer thickness of the porcelain at this location was found to be 0.925 mm, as measured from Scanning Electron Microscopy (SEM) images. Data at the extreme ends of this scan were excluded from the PDF analysis. In the case of data collected closest to the YPSZ substrate, Bragg peaks from the zirconia were observed, whereas

the scattered intensity dropped significantly at the extreme of the porcelain side. At both extremes, this meant that the PDF data generated was not of the necessary quality for detailed analysis.

2.2.2. PDF processing

One of the important considerations that needs to be taken into account when performing amorphous PDF analysis is the presence of crystalline material within the diffraction pattern. Within the study by Lunt et al. a crystalline content of less than 1% was present within the porcelain, and therefore masking of these peaks was performed during the data processing stage [37]. Within the present study several similar Bragg peaks were identified within the data, however the intensity and number of these peaks was found to be sufficiently low as to not noticeably influence the azimuthally integrated profiles. In order to quantify this effect, Rietveld refinement was performed on the scattered data in order to determine that the crystalline content was less than 0.1% on average, with no spatial trends in crystallite concentration within the veneer. As a result, the influence of crystallites on the experimental results was expected to be significantly lower than the confidence limits associated with other stages of the data interpretation procedure.

The software package DAWN [39] was used to process the 2D images in order to provide 1D amorphous scattering profiles in the horizontal and vertical directions. In order to do this azimuthal integration was performed from the centre of the diffraction pattern to a momentum transfer Q of 25.1Å^{-1} at an angle relative to the vertical. The vertical profile was obtained by averaging the integrated distributions from −15° to 15° and 165° to 195°, and the horizontal was obtained by averaging the distributions from 75° to 105° and 255° to 285°. Integrating using this approach greatly improves the statistics of the 1D profiles obtained, at the expense of the averaging over small variations expected in azimuthal strain (with a maximum error of 2.3% expected).

The segmented 1D scattering data from DAWN was further processed using the software GudrunX [40] in order to correct for background, Compton, and multiple scattering, as well as beam attenuation. Using the approach published by Keen [41] the resulting total scattering function S(Q) was next Fourier transformed to produce the PDF which has a form similar to Fig. 2 in the article by Lunt et al. [37], where r is the interatomic distance.

2.2.3. PDF strain calibration

The resulting pair distribution function, $G(r)$, is a quantitative histogram of interatomic distances between a pair of atoms, and the area of the peaks are related to the coordination of the atoms [42]. The PDF can therefore give structural information about the atomic bonding environment, even for amorphous substrates. Even in the absence of a complete structural model for a material the deviations in the PDF peak positions and intensities provides a quantitative indication of the alteration in the local structural lengths within the material.

As demonstrated by Lunt et al. in their study [37], the application of externally applied strains through the use of a loading rig, result in PDF peak shifting in dental porcelain. This behaviour can be considered to be analogous to the Bragg peak shifting response observed in crystalline materials under applied strain [43]. In the case of Bragg diffraction, X-ray powder diffraction produces Debye-Scherrer rings that correspond to 1D profiles with sharp, clearly defined peaks after azimuthal integration. These peaks can be individually fitted to provide reliable estimates of peak centres and lattice parameters, and thereby lattice strain for crystallite planes with a given Miller index [44]. Alternatively, full refinement of the diffraction pattern can be performed to provide an overall estimate of the unit cell dimensions (lattice parameters) of the material. This is a global minimisation problem that takes into account the peak centres (and shape) of multiple peaks to derive the parameter descriptors of the crystalline lattice.

For PDF data, peak positions also change due to the local displacement of atoms under the application of macroscopic strain. However, not all peaks displace to the same extent: the amount of peak shift depends on the extension and rotation of the bonds that define the particular interatomic distance. The broad peak shape observed in PDF data of amorphous substances means that peak overlap, coupled with differences in the amount of shift between individual peaks, may reduce the certainty with which the centre of a single peak can be determined. Statistical noise in the collected diffraction pattern, particularly at high values of Q where the scattering signal is weak, may also induce aberrations in the peak centre position determination at lower radial distances. Typically this is not a problem as the peak shifts are small [45], and when matching structural models to entire patterns, this behaviour can be averaged out over multiple peaks; this means that an approach equivalent to single peak fitting and the associated identification of strain is imprecise and ultimately forms an unreliable measure of strain. However, in order to overcome this limitation, an approach based on multiple peak fitting in order to identify a single average measure of strain is sufficiently precise as to provide a reliable measure. This fundamental approach forms the basis of strain quantification used here.

In order to provide estimates of the macroscopic strain distribution within the porcelain veneer, the impact of macroscopic strain $\left(\varepsilon^{M}\right)$ on the PDF profile of porcelain needs to be determined. In order to describe this relationship most effectively, we begin by introducing the concept of atomic strain $\left(\varepsilon_k^A\right)$ within amorphous materials [25]. The value of ε_k^A is dependent upon the atomic pair under consideration, which corresponds to a particular peak (k) within the PDF profile. This descriptor can be considered the equivalent of lattice strain within crystalline materials and is given by the expression:

$$\varepsilon_k^A = \frac{r_k - r_k^0}{r_k^0}, \tag{2}$$

where r_k is the fitted radial peak centre position at for the k^{th} peak and r_k^0 is the equivalent unstrained radial peak centre of that peak, i.e. when the applied macro strain is zero. As part of the study by Lunt et al. quantification of r_k^0 and the associated standard deviation, $\sigma_{r_k^0}$, was performed on 39 peaks [37]. Some of these peaks were found to show limited correlation between macroscopic strain and peak centre position. Therefore, only those peaks with a correlation coefficient(R_k) value greater than ~2/3 were analysed further. As a result, estimates

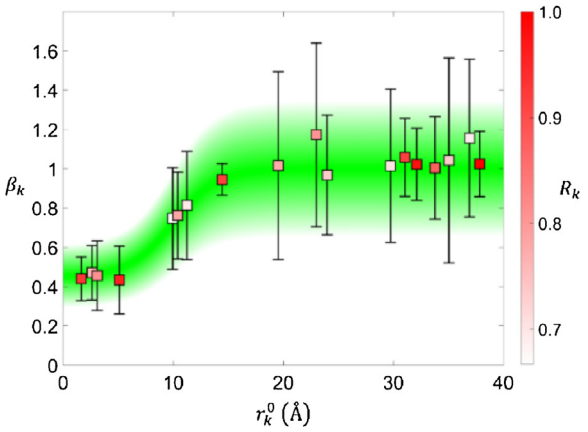

Fig. 2 – Constant of proportionality between atomic and macroscopic strain (β_k) against the unstrained radial peak centre position r_k^0 as published by Lunt et al. [33]. The correlation coefficient between atomic and macroscopic strain at each point (R_k) is indicated by the marker colour and the 95% confidence interval for each value is indicated by error bars. A region highlighting the general trends in the data the associated confidence intervals is shown in green.

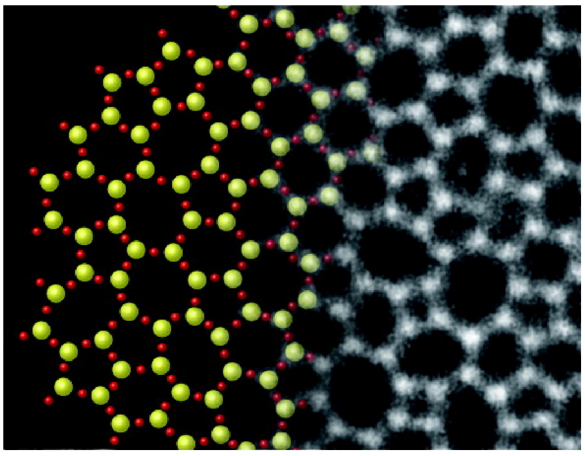

Fig. 3 – Simulated (left, colour) and experimentally determined (right, greyscale) atomic arrangements in amorphous silica (green/lighter coloured spots = silicon atoms, red/darker coloured regions = oxygen atoms). Note the presence of atomic rings consisting of 4-8 silicon atoms [42]. (For interpretation of the references to colour in this figure legend, the reader is referred to the web version of this article.)

of r_k^0 for 18 peaks covering r values in the range 1.64–37.84 Å were obtained. These can be used to quantify ε_k^A from estimate of r_k obtained from peak fitting of the PDF data in this study.

Once estimates of the atomic strain have been obtained for each peak, the relationship between ε_k^A and the macroscopic strain can be exploited to estimate the macroscopic strain for each peak:

$$\varepsilon_k^M = \varepsilon_k^A / \beta_k \tag{3}$$

Here, β_k is the constant of proportionality between the two measures of strain for a given peak k. For peaks at large radial distances the value of atomic strain must tend towards that of macroscopic strain, and therefore the $\lim_{k\to\infty} \beta_k = 1$.

For the 18 peaks under consideration, estimates of the standard deviation of β_k, σ_{β_k}, were also quantified and published by Lunt et al. as shown in Fig. 2.

The transition from the reduced value of $\beta_k \sim 0.45$ for the near neighbours to $\beta_k \sim 1$ for atomic pairs separated by ~20 Å or more has been explained in [37] by identifying the dominance of bond rotation over bond stretching for near neighbours. It is particularly interesting to discuss these findings in the context of the nature of order and disorder present in amorphous materials.

Fig. 3 illustrates the results of the study by Huang et al. that reveal the structure of 2D layer of amorphous silica on graphene substrate [46]. The preponderance of four- to eight-membered silicon rings is evident in the structure. Further interpretation of the data is shown in Fig. 4 in the form of radial pair distribution function $G(r)$ for the crystalline (a) and amorphous (b) silica. It is apparent that at the radial distances below ~10 Å both crystalline and amorphous forms show strong peaks indicating the presence of strong Si—O bonds, as well as second neighbour distances that correspond to Si—O—Si and O—Si—O arrangements. These rigid groups correspond to the Short Range Order (SRO) in the atomic arrangement that is present in both structures. In the current interpretation, (as shown in Fig. 2) this corresponds to the 'stiff' (low β_k) strain response of the pairwise peaks. In the Medium Range Order (MRO) range between ~10 and 20 Å, whilst crystalline modification retains the presence of sharp peaks, in the amorphous configuration the peaks become progressively broader and lower in magnitude. This is reflected in the intermediate values of β_k observed by Lunt et al. [37]. Finally, the apparent absence of the Long Range Order (LRO) in amorphous silica results in the convergence of β_k values to unity for pairwise distances greater than ~20 Å.

These observations allow further interpretation in the light of Fig. 4c that reveals the presence of five- to eight-membered rings of Si atoms within amorphous silica. The mean diameter of an n-membered ring is approximately equal to nÅ. We draw the conclusion that in silica, the SRO structure is defined by these rings, whose principal deformation mode corresponds to ring distortion, that we describe in [37] in terms of Si—O—Si bond rotation. At interatomic distances in excess of 10 Å, transition to MRO occurs, with LRO setting in at the distances that correspond to ~3 ring diameters, which is reflected in the β_k values converging to unity.

2.2.4. *PDF strain quantification*

Precise knowledge of β_k values such as those provided by Lunt et al. [37] can serve as calibration for the quantification of unknown macroscopic strains from PDF measurements. This requires the quantification of the atomic strains through PDF peak fitting and β_k, as shown in Eq. (3). In this study, following the data collection routine outlined in Section 2.2.1, this approach has been used to provide ε_k^M estimates within the

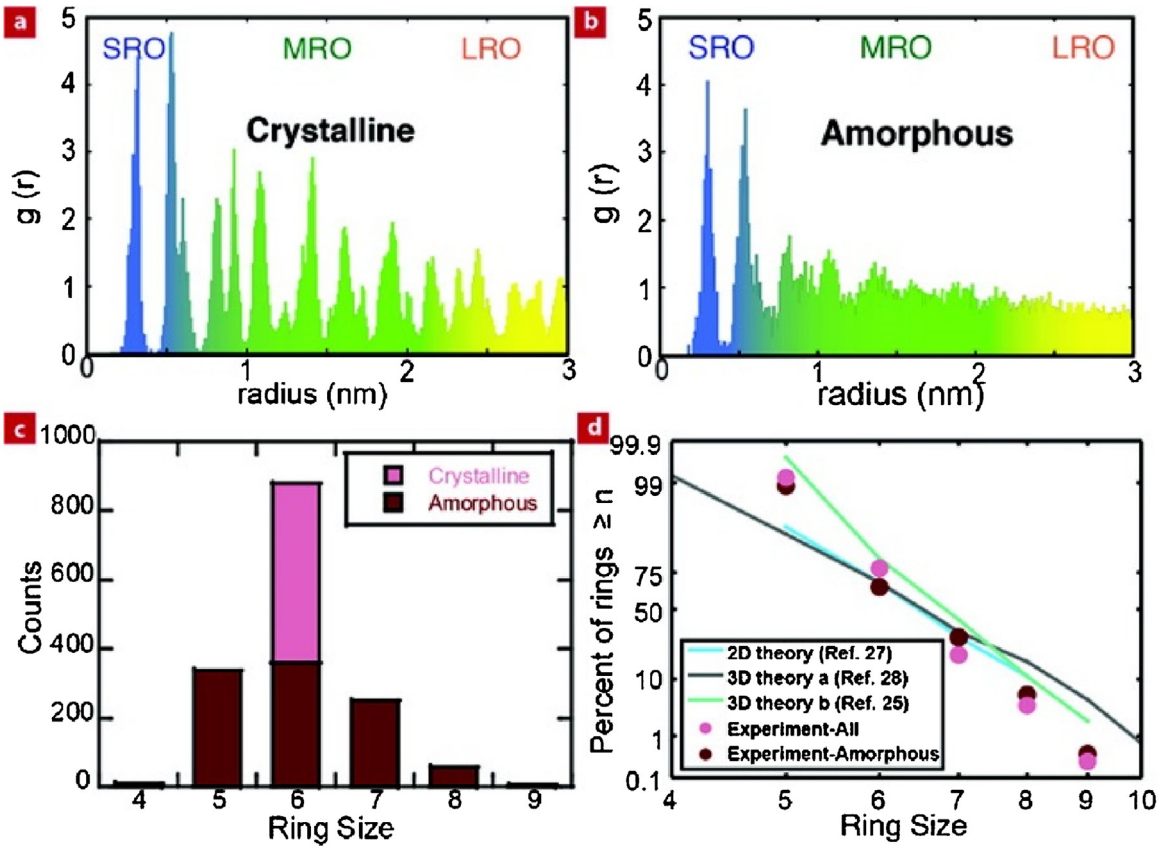

Fig. 4 – (a) and (b) Illustrate the radial pair distribution function G (r) for crystalline and amorphous polytypes of 2D layer of silica on graphene, based on experimental observation [42]. (c) The number of counts for n-membered atomic rings of different 'size' (number of Si atoms). (d) Percentage of n-membered rings within amorphous silica.

veneer from the ε_k^A determined experimentally, as outlined below.

Despite the similarities in elemental composition between Cerec 2 VITABLOC® Mark II and e.max Ceram, differences were observed within the PDF patterns of the two materials. These differences are likely to be associated with the differing manufacturing and thermal processing routes applied to the two compositions. Examination of the PDF profiles obtained from the two porcelain types revealed however that for small values of r, strong similarities were observed. For this reason the remainder of the residual strain quantification analysis was focused on the range of interatomic distances $r \leq 5.5$ Å. Within this radial distance, seven distinct peaks were observed which correspond to the nearest 1st and 2nd neighbour distances, primarily between Si and O atoms. It was found that four of these peaks showed good correlation between macroscopic and atomic strains, as shown in Table 1.

Gaussian peak fitting was performed on the data collected from the porcelain veneer in directions parallel and perpendicular to the YPSZ-porcelain interface. The peak centre r_k and confidence interval, σ_{r_k}, were obtained for each of the four peak positions given in Table 1. A small correction factor (0.73%) was applied to the r_k values in order to accommodate minor experimental misalignment, or slight differences between the porcelain types, as outlined in the Appendix A.

Table 1 – Peak centre, correlation coefficient and macro-atomic strain proportionality coefficient for the four PDF peaks used in the porcelain veneer macroscopic strain quantification. The atomic pairs corresponding to each peak have been identified.

Pairs	k	r_k^0 (Å)	$\sigma_{r_k^0}$ (Å)	β_k	σ_{β_k}	R_k
Si—O	1	1.65	9.31×10^{-6}	0.44	5.73×10^{-2}	0.88
O—O	2	2.64	3.64×10^{-5}	0.47	7.07×10^{-2}	0.76
Si—Si	3	3.10	4.44×10^{-5}	0.45	9.03×10^{-2}	0.79
Si—Si/O—O[a]	4	5.11	2.17×10^{-5}	0.43	8.17×10^{-2}	0.90

[a] The peak at $r = 5.11$ corresponds to a combination of the peaks of the 2nd nearest neighbours of silicon and oxygen.

Eqs. (2) and (3) were combined in order to convert the peak centre positions to macroscopic strain estimates for each peak:

$$\varepsilon_k^M = \frac{r_k - r_k^0}{\beta_k r_k^0}. \tag{4}$$

The standard deviation of these macroscopic strain estimates were also obtained using the expression:

$$\sigma_{\varepsilon_k^M} = \frac{\sqrt{\beta_k r_k^0 \left(\sigma_{r_k}^2 + \sigma_{r_k^0}^2\right) + \sqrt{\left(r_k - r_k^0\right)^2 \left(r_k^0 \sigma_{\beta_k}^2 + \beta_k \sigma_{r_k^0}^2\right)^2}}}{\beta_k r_k^0}. \tag{5}$$

In order to determine a single parallel and perpendicular strain estimate at each position, a weighted average of the four strain values was obtained using the standard deviation of each estimate.

2.3. Ring-core analysis

2.3.1. FIB milling

The sequential spatially resolved ring-core FIB milling and DIC technique [16,27,29] was applied across the surface of the prosthesis cross section. This approach was intended to provide comparative measurement validation of strain within the porcelain veneer at the locations previously investigated by PDF methods.

The 2 mm prosthesis cross section was mounted onto an SEM stub using silver paint and 5 nm of gold-palladium was sputtered onto the surface of the sample to reduce the impact of charging during SEM imaging and FIB milling. The sample was then placed into the Tescan Lyra 3XM FIB-SEM at the Multi Beam Laboratory for Engineering Microscopy (MBLEM), Oxford, UK. Tilt corrected 2048 × 2048 pixel SEM images were collected at a working distance of 9 mm and an accelerator voltage of 5 kV, using the configuration previously reported in the literature [27]. In order to generate the high contrast surface necessary for effective DIC, a single pass of the 30 keV ion beam was used to create a random surface texture pattern as shown in Fig. 5. This approach, in combination with an automated brightness and contrast routine, has previously been shown to give a stable and effective contrast generation technique which is more reliable than deposition based contrast [29,47,48].

Following the calibration of the FIB milling rate of porcelain, the first ring-core milling position was selected to lie at the interface between porcelain and YPSZ. A 5 μm diameter core and 1.5 μm trench width were selected as a balance between maximising the resolution of the measurements on one hand, and minimising the error associated with the strain measurement on the other. A nominal milling depth increment of 100 nm was implemented between the collection of each successive SEM image, and a total of 50 images were collected in around 35 min. This process was repeated across the entire porcelain veneer with the lateral position increment of 50 μm between successive measurement points. For a 5 μm diameter core, a step size of 50 μm is known to correspond to a maximum induced relief of less than 0.5% at the successive measurement point [27] which is much less than the typical error bounds associated with this technique. The final point was measured at a distance of 20 μm from the previous position in order to provide a measurement as close as possible to the edge of the sample.

2.3.2. Digital image correlation for residual strain quantification

Following the application of the ring-core FIB milling and SEM image collection routine, residual strain quantification was performed in directions parallel and perpendicular to the YPSZ-porcelain interface using a modified version of the MATLAB DIC code developed by Eberl [49]. The fundamental principles behind approach have been discussed in detail elsewhere in the literature [29,50,51] and therefore only the specific parameters implemented in this study are included here.

Low resolution DIC (reduction factor = 5) was initially applied to all image sets to correct for any bulk drift induced during milling [52]. Several thousand 'DIC markers' or image subsets were then placed across the central 60% of the core region where strain relief has previously been shown to be uniform [53]. A correlation window size of 10 by 10 pixels was used to maximise the precision of the tracking while minimising boundary effects [54]. Automated 2D tracking of the markers was performed for each image set in order to provide insight into the displacement (and thereby strain relief) of each point as a function of milling depth. Outlier removal of poorly tracked markers was implemented using the multi-stage routine developed by Lunt et al. [29]; correlation coefficient thresholding was first used to remove markers in which noise had reduced this measure of quality below 0.5. Peak position standard deviation thresholding was next used to remove markers with a standard deviation 1.5 times greater than the mean value. Finally, any outliers to the expected displacement field were removed by thresholding markers at a distance greater than 1.5 times the average offset. This process ensured that only the well-tracked markers were used in the strain quantification analysis.

Next, linear total least squares fitting was used to obtain the estimates of strain relief at each milling depth in directions parallel and perpendicular to the YPSZ-porcelain interface. The resulting plots of strain relief against image number were then fitted with the Finite Element (FE) relief 'master curve' outlined by Korsunsky et al. [16]. This process provides estimates of $\Delta\varepsilon_{\infty}^{0^{\circ}}$ and $\Delta\varepsilon_{\infty}^{90^{\circ}}$, the full strain relief at infinite depth in directions parallel (0°) and perpendicular (90°) to the interface. These two measurements represent the strain change within the core during the milling process and are the negative of the residual strains originally present within the material, i.e. an increase in the core size (positive strain change) is indicative of a pre-existing compressive residual strain.

During this entire process, care was taken to propagate all sources of error in order to provide reliable confidence bounds on each of the residual strain relief estimates. This process combined the confidence intervals associated with each of the DIC markers and the multiple fitting processes implemented in this analysis, as previously reported elsewhere [29].

3. Results

The estimates of strain variation within the porcelain veneer obtained using PDF analysis and the FIB milling and DIC approach are shown as a function of distance from the YPSZ-porcelain interface in Fig. 6. Strains in directions parallel and perpendicular to the interface have been plotted separately and are shown in Fig. 6a and b, respectively.

In order to draw reliable comparisons between the strain measurements obtained, consideration of the gauge volumes and stress states associated with the two techniques is required. The ring-core geometry generated as part of the FIB milling and DIC technique has a well-defined gauge volume that is contained within the 5 μm diameter core. This approach is a surface based technique and therefore the stress state con-

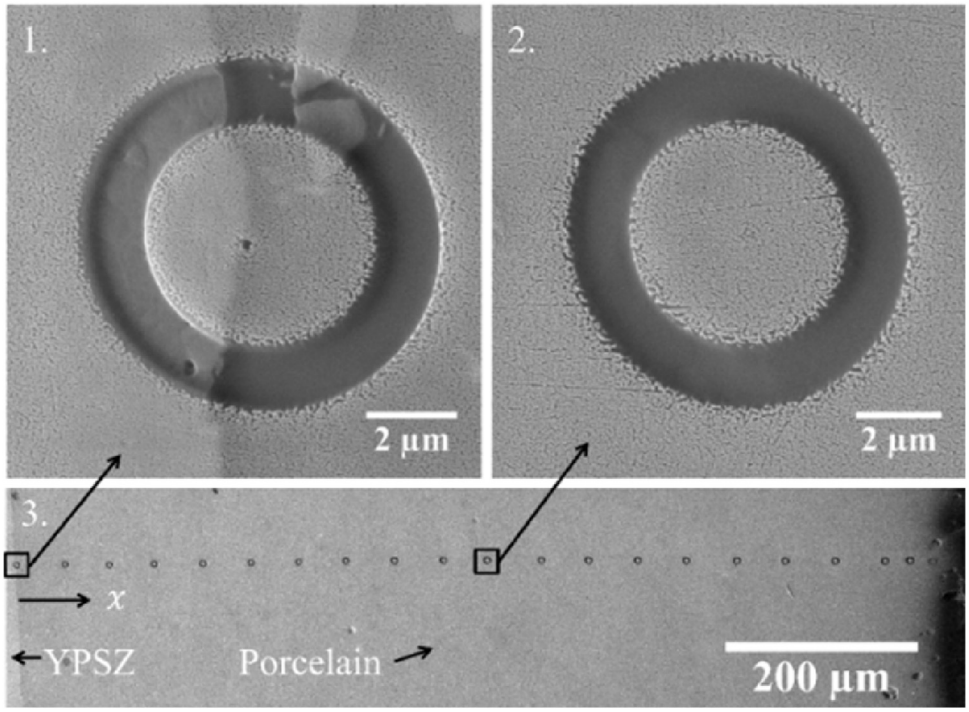

Fig. 5 – SEM micrographs of ring-core FIB milling positions. 1. Milling position at the YPSZ-porcelain interface. 2. Typical example of ring-core milling from the centre of veneer. 3. Overview of all milling positions.

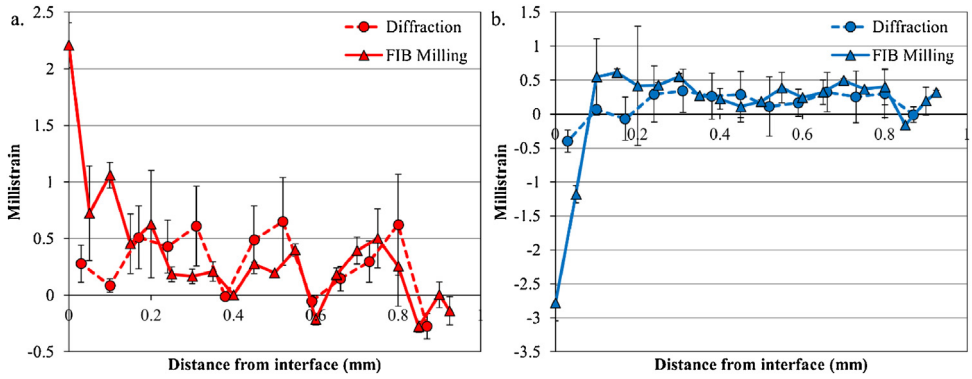

Fig. 6 – Strain variation within the porcelain veneer as a function of distance from the interface. The results from PDF analysis and FIB milling and DIC are shown in directions (a) parallel and (b) perpendicular to the YPSZ-porcelain interface. The error bars indicate the 95% confidence intervals of each data point.

tained with the measured region can be well approximated by plane stress conditions.

In the case of the PDF analysis study, the gauge volume has a cross section equal to the size of the incident beam ($\emptyset = 70\ \mu$m) and is representative of an average through the thickness of the sample (2 mm). Therefore, the sampled volume contains both the near-surface region (which can be approximated by plane stress conditions) and the region far from the sample surface (close to plane strain conditions). The difference between the near-surface and through-thickness average stress states has been discussed in depth elsewhere [34,55]. A good approximation for the difference between plane stress and plane strain (under initially equivalent eigenstrain) is given by the square of Poisson's ratio. This means that the maximum difference between the stress states measured using the two techniques is less than ≈4% [35].

In the case of strains in a direction parallel to the interface (Fig. 6a), it can be seen that despite the differing gauge volumes, the distributions show several similar trends. The porcelain is on average in a state of mild tension and within the first ~0.6 mm from the edge of the sample. A periodic distribution with a spacing of 0.2–0.3 mm is observed. This repeating pattern has maximum tensile strain of approximately 0.5×10^{-3} and a maximum compressive strain of $\sim 0.25 \times 10^{-3}$ is also present within the outer 50–75 µm at the edge of the sample. In contrast to this, tensile strains are present in the YPSZ-porcelain near interface region.

Examination of the strain distributions obtained in a direction perpendicular to the interface (Fig. 6b) reveals that the porcelain is predominately in a constant state of mild tension of $\sim 0.5 \times 10^{-3}$. At the YPSZ-porcelain interface, a $\sim 100\,\mu m$-wide band of compressive strain is observed and at the free edge a region of low magnitude compressive and tensile strains are present.

For both strain orientations it can be seen that the strain estimates obtained through PDF analysis are generally less precise than those obtained using the FIB milling and DIC approach. Despite this, the majority of PDF strain estimates show 95% confidence interval overlap with neighbouring FIB milling and DIC strain estimates, suggesting that realistic approximations of the strain state have been identified.

4. Discussion

Throughout this article the concept of residual strain i.e. the change in the atomic spacing relative to the stress free state has been investigated and measured. This parameter is intrinsically related to residual stress, which expresses the force per unit area that is associated with this strain state. Conversion between these two measures can be performed by making use of Young's modulus and Poisson's ratio and well-established relationships [50,55]. Despite this, for residual strains within a given plane, the relationship with residual stress is dependent upon the out of plane state, which at the two extremes can be well approximated by plane stress and plane strain conditions. Indeed, these two serve as upper and lower bounds on the residual stress estimates for a given strain state, and many techniques (such as hole drilling) intrinsically rely upon these approximations to provide stress estimates [56]. A similar approach could be used to provide residual stress estimates from the residual strain estimates provided by the ring-core approach in this study as the gauge volume is at the surface of the sample, and therefore plane stress conditions serve as a good approximation. However, as outlined in Section 3, the gauge volume sampled by the PDF approach contains regions both the surface and the bulk, which are best approximated by plane stress and plane strain conditions respectively. For this reason, the residual strain to stress conversion is less straightforward, and at best can provide upper and lower bounds of these values. Therefore, in this study this conversion has not been performed and instead, a direct and more valid comparison with the fundamental descriptor of the structure i.e. residual strain has been performed.

Examination of the residual strain profiles reveals that in general the PDF and FIB based approaches give results that are comparable both in terms of magnitude and in terms of spatial variation. As outlined in Section 3, the maximum error associated with the difference between the plane strain and plane stress approximations is expected to be of the order of 4%, which is significantly lower than the average 95% confidence intervals obtained experimentally. This calculation is based on the approximation that a uniform residual strain state exists perpendicular to the plane of the sample, and significant deviations between the results obtained by the two techniques would indicate that this assumption was invalid. However, this appears not to be the case, thereby suggesting that a valid comparison can be drawn.

The region which appears to show maximum difference between the two strain profiles is contained within the first 0.2 mm of the YPSZ-porcelain interface. This region is known to be the most influenced by coefficient of thermal expansion mismatch between the two materials [11] and contains the point at which failure of the system is most likely to occur [57]. The large gradients in residual stress expected at this location ensure that the approximation of uniform stress through thickness is least reliable.

The point of maximum difference between the two profiles occurs at the interface location where the FIB milling and DIC result suggests a state of high magnitude shear strain. Although similar high magnitude strains have previously been reported close to the interface location [17], this is the first reported application of ring-core residual stress analysis with a bi-material core. Material interaction within the core and non-uniform relaxation will influence the strain measurement at this location. Therefore, firm conclusions cannot be drawn from this position without further modelling of this distribution of mechanical properties.

In order to understand the likely origins of the residual strain state of the porcelain, the manufacturing route of the veneer needs to be considered. To build up the required shape multiple layers of porcelain slurry are applied and heated to between 600–750 °C for a relatively short time period (2 min). Furnace cooling is then used to return the coping to room temperature over a period of several tens of minutes. The spatial period of the tensile and compressive strains observed within the veneer corresponds closely to the typical thickness of these porcelain layers, and suggests that this is the origin of the strain variation in the veneer.

Characteristic tensile and compressive strain distributions similar to those observed in the multi-layer veneer are known to be induced in the surface of quenched metallic components [58]. This strain state is induced by the surface of cooling at a faster rate than the bulk material and the associated solidification which occurs before that of the underlying bulk material. Continual cooling of the component leads to shrinkage of the bulk and the induction of compressive strains in the surface layer. Stress equilibrium then ensures that tensile strains are induced in these sub-surface regions upon full solidification.

In the case of the multi-layered porcelain veneer, this process occurs multiple times during the manufacture of the prosthesis, and therefore a characteristic alternating pattern of tension and compression is induced in the porcelain. Similar tensile and compressive strain variations have previously been observed in veneers of the same overall thickness, with the period of the cyclic behaviour showing a strong dependence upon the thickness of the applied layers [15]. Another important consideration in this manufacturing process is the impact of repeated exposure to sintering temperatures of the underlying veneer layers. It can be seen that the layers nearest the YPSZ are exposed to larger number of thermal cycles, which may facilitate relaxation of the stress state within the veneer through porcelain creep [4,59]. Porcelain creep induced nanovoiding has recently been characterised and observed at the YPSZ-porcelain interface for the first time, providing further evidence for this behaviour [60] and would result in lower

magnitude, smoother strain variation similar to that identified between 0.2 and 0.4 mm from the interface.

Examination of the residual strains in the direction perpendicular to the interface indicates tensile residual stress acting in this orientation. Uniform tensile residual stresses within porcelain veneers have been widely reported in the literature [11,17,61]. This response is believed to be associated with the combined effects of thermal expansion mismatch and the geometry produced during veneer manufacture.

The final stage of prosthesis manufacture involves manual multi-stage polishing with decreasing sizes of grinding medium in order to produce an aesthetically pleasing and lustrous finish. Polishing of this type is known to induce near-surface compressive stresses in prosthesis materials [62] and therefore may explain the compressive strains observed at the surface in both orientations.

Improved understanding of the residual stress within the porcelain veneer of YPSZ dental prostheses is critical in minimising the failure rates of these components, and as such has been discussed at depth within the literature [15,17,56,61,63]. The insights provided by the experimental characterisation performed in this study serve as key inputs to effective analytical models and simulations of the production of these components [64,65]. These approaches are being used to tailor the production parameters and treatments applied in order to minimise prosthesis failure through chipping. This methodology has already resulted in improvement to the reliability of prosthesis by improved design [2], and continues to be a major focus of dental implant research.

The PDF approach is a new non-destructive residual strain quantification approach, and such it is important to discuss its relevance and suitability against existing residual stress/strain measurement techniques that have been outlined comprehensively in the literature [27,66,67]. There are several advantages of the methodology, which ensures that it has excellent applicability. Firstly, this approach provides insight into residual strain variation at the microscale. This resolution far surpasses that of conventional destructive and semi-destructive techniques such as hole-drilling [68], the slitting method [69] and the contour method [70], which although applicable to amorphous materials, are typically capable of resolving stresses at a spatial resolution in the order of millimetres.

It is well known that microscale residual stress mapping is possible by making use of advances in the focusing optics of X-ray radiation in recent decades [71]. To-date, these methods all rely upon the sharp and well-defined Bragg peaks present in the diffraction patterns of crystalline materials and therefore cannot be applied to amorphous materials. In contrast, the PDF residual stress technique is applicable to materials composed of a disordered atomic arrangement, and therefore a new spectrum of samples and field of investigation will be possible by making use of this technique.

The only other techniques that have previously been able to resolve the residual stress variation at the microscale within amorphous systems, have been those techniques based on the introduction of microscale traction free surfaces through FIB milling and the assessment of the resulting relief through DIC [27]. Despite the many advantages of these methods, these approaches are intrinsically surface based methods, and 'through sample' averaging is not possible using these techniques. Therefore, for the first time, the PDF approach therefore offers the ability to probe the residual strain variation within the bulk regions of an amorphous substrate and provide insights that are critical in improving our understanding of a broad spectrum of materials and applications.

5. Conclusion

In this study, a new technique for residual strain evaluation in amorphous materials based on PDF analysis has been developed and applied to a sample of commercial interest: porcelain veneer deposited on a partially stabilised zirconia dental prosthesis. This method offers a new tool for improved characterisation of strain distributions within a broad range of amorphous materials, including bulk metallic glasses and polymers. Despite the many benefits of this approach, the results have highlighted that in order to produce reliable strain estimates, careful calibration is required.

Validation of the residual strain profiles within the porcelain veneer has been performed using the sequential ring-core FIB milling and DIC approach. The results obtained from this relatively new technique showed good comparison with those obtained by diffraction analysis of amorphous material, and have further demonstrated that this semi-destructive approach offers a rapid and precise cross-validation technique for problems of this type.

In the direction parallel to the interface, the multi-stage veneering process used to manufacture the prosthesis has been shown to induce oscillatory tensile and compressive strains, while a purely tensile residual strain was observed in the perpendicular direction. At the interface between YPSZ and porcelain, the highest magnitude shear based residual strains are present. This is likely to be related to the shear based tetragonal to monoclinic YPSZ phase transformation and, when combined with external loading, leads to preferential porcelain chipping at this location.

The insights gained in this study can be used to provide inputs to analytical and finite element modelling of prosthesis manufacture and thereby suggest new prosthesis manufacturing routes, e.g. in terms of the choice of veneer layer thickness or sintering temperatures. In turn, these can be used to minimise the residual strain build up and reduce the likelihood of failure in future designs.

Funding sources

This work was supported by the European Project EU FP7 project iStress (604646). Further support was provided by Diamond Light Source, UK via access funding to beamline I15 (proposal EE9106-1).

Data statement

Additional data can be accessed via ORA (http://ora.ouls.ox.ac.uk). Requests for any material samples or specimens described in this manuscript should be directed to the corresponding author.

Appendix A. Scaling of r_k values

Initial examination of the macroscopic strain estimates obtained by this analysis revealed that although the variation between terms seemed realistic, the magnitude of the estimates was far beyond the yield strain of porcelain. Similar unrealistic strain magnitude offsets of this type can be found during lattice strain quantification of crystalline substrates due to incorrect value of the material-dependent unstrained lattice parameter d° [72]. One approach applied to overcome this problem has been to compare the lattice strain variation with distributions obtained by other independent experimental techniques, for example the ring-core FIB milling and DIC approach [27,73]. Adopting this approach, Eq. (4) was modified to include a correction factor (γ) on r_k:

$$\varepsilon_k^M = \frac{\gamma r_k - r_k^0}{\beta_k r_k^0}. \quad (6)$$

Optimisation of this scaling factor was performed by comparison with the strain estimates obtained in Section 2.3.2 in order to give a single value of $\gamma = 1.0073$ for the entire data set. This parameter may be indicative of the minor elemental and microstructural differences between the two porcelain types examined in this study, or alternatively may indicate a small (1.9 mm) error between the sample and calibrant position.

REFERENCES

[1] Denry I, Kelly JR. State of the art of zirconia for dental applications. Dent Mater 2008;24:299–307, http://dx.doi.org/10.1016/j.dental.2007.05.007.

[2] Raigrodski AJ, Hillstead MB, Meng GK, Chung K-H. Survival and complications of zirconia-based fixed dental prostheses: a systematic review. J Prosthet Dent 2012;107:170–7, http://dx.doi.org/10.1016/S0022-3913(12)60051-1.

[3] Schmitt J, Holst S, Wichmann M, Reich S, Gollner M, Hamel J. Zirconia posterior fixed partial dentures: a prospective clinical 3-year follow-up. Int J Prosthodont 2009;22:597–603.

[4] Lunt AJG, Mohanty G, Ying S, Dluhoš J, Sui T, Neo TK, et al. A comparative transmission electron microscopy, energy dispersive x-ray spectroscopy and spatially resolved micropillar compression study of the yttria partially stabilised zirconia — porcelain interface in dental prosthesis. Thin Solid Films 2015;596:222–32, http://dx.doi.org/10.1016/j.tsf.2015.07.070.

[5] Lunt AJG, Mohanty G, Neo TK, Michler J, Korsunsky AM. Microscale resolution fracture toughness profiling at the zirconia-porcelain interface in dental prostheses. Micro + nano materials, devices, and systems, vol. 9668. International Society for Optics and Photonics; 2015, http://dx.doi.org/10.1117/12.2199217. p. 96685S.

[6] Tholey MJ, Swain MV, Thiel N. SEM observations of porcelain Y-TZP interface. Dent Mater 2009;25:857–62, http://dx.doi.org/10.1016/j.dental.2009.01.006.

[7] Kawai Y, Uo M, Watari F. Microstructure evaluation of the interface between dental zirconia ceramics and veneering porcelain. Nano Biomed 2010;2:31–6, http://dx.doi.org/10.11344/nano.2.31.

[8] Al-Amleh B, Neil Waddell J, Lyons K, Swain MV. Influence of veneering porcelain thickness and cooling rate on residual stresses in zirconia molar crowns. Dent Mater 2014;30:271–80, http://dx.doi.org/10.1016/j.dental.2013.11.011.

[9] Fardin VP, Bonfante EA, Coelho PG, Janal MN, Tovar N, Witek L, et al. Residual stress of porcelain-fused to zirconia 3-unit fixed dental prostheses measured by nanoindentation. Dent Mater 2018;34:260–71, http://dx.doi.org/10.1016/j.dental.2017.11.013.

[10] Inokoshi M, Zhang F, Vanmeensel K, De Munck J, Minakuchi S, Naert I, et al. Residual compressive surface stress increases the bending strength of dental zirconia. Dent Mater 2017;33:e147–54, http://dx.doi.org/10.1016/j.dental.2016.12.007.

[11] Baldassarri M, Stappert CFJ, Wolff MS, Thompson VP, Zhang Y. Residual stresses in porcelain-veneered zirconia prostheses. Dent Mater 2012;28:873–9, http://dx.doi.org/10.1016/j.dental.2012.04.019.

[12] Mochales C, Maerten A, Rack A, Cloetens P, Mueller WD, Zaslansky P, et al. Monoclinic phase transformations of zirconia-based dental prostheses, induced by clinically practised surface manipulations. Acta Biomater 2011;7:2994–3002, http://dx.doi.org/10.1016/j.actbio.2011.04.007.

[13] Manicone PF, Rossi Iommetti P, Raffaelli L. An overview of zirconia ceramics: basic properties and clinical applications. J Dent 2007;35:819–26, http://dx.doi.org/10.1016/j.jdent.2007.07.008.

[14] Seghi RR, Denry IL, Rosenstiel SF. Relative fracture toughness and hardness of new dental ceramics. J Prosthet Dent 1995;74:145–50, http://dx.doi.org/10.1016/S0022-3913(05)80177-5.

[15] Zhang Y, Allahkarami M, Hanan JC. Measuring residual stress in ceramic zirconia-porcelain dental crowns by nanoindentation. J Mech Behav Biomed Mater 2012;6:120–7, http://dx.doi.org/10.1016/j.jmbbm.2011.11.006.

[16] Korsunsky AM, Sebastiani M, Bemporad E. Focused ion beam ring drilling for residual stress evaluation. Mater Lett 2009;63:1961–3, http://dx.doi.org/10.1016/j.matlet.2009.06.020.

[17] Sebastiani M, Massimi F, Merlati G, Bemporad E. Residual micro-stress distributions in heat-pressed ceramic on zirconia and porcelain-fused to metal systems: analysis by FIB–DIC ring-core method and correlation with fracture toughness. Dent Mater 2015;31:1396–405, http://dx.doi.org/10.1016/j.dental.2015.08.158.

[18] Snyder RL. X-ray diffraction. In: X-ray characterization of materials. Wiley-Blackwell; 2007. p. 1–103, http://dx.doi.org/10.1002/9783527613748.ch1.

[19] Hastings JB, Thomlinson W, Cox DE. Synchrotron X-ray powder diffraction. J Appl Cryst 1984;17:85–95, http://dx.doi.org/10.1107/S0021889884011043.

[20] Zhang H, Sui T, Salvati E, Daisenberger D, Lunt AJ, Fong KS, et al. Digital image correlation of 2D X-ray powder diffraction data for lattice strain evaluation. Materials 2018;11:427.

[21] Bates S, Zografi G, Engers D, Morris K, Crowley K, Newman A. Analysis of amorphous and nanocrystalline solids from their X-ray diffraction patterns. Pharm Res 2006;23:2333–49, http://dx.doi.org/10.1007/s11095-006-9086-2.

[22] Feng R. Modelling atomic structure in amorphous solids and x-ray diffraction. Lap Lambert Academic Publishing GmBh KG; 2012.

[23] Poulsen HF, Wert JA, Neuefeind J, Honkimäki V, Daymond M. Measuring strain distributions in amorphous materials. Nat Mater 2005;4:33.

[24] Ice G. Amorphous materials: characterizing amorphous strain. Nat Mater 2005;4:17–8, http://dx.doi.org/10.1038/nmat1302.

[25] Huang YJ, Khong JC, Connolley T, Mi J. In situ study of the evolution of atomic strain of bulk metallic glass and its

effects on shear band formation. Scr Mater 2013;69:207–10, http://dx.doi.org/10.1016/j.scriptamat.2013.03.016.
[27] Lunt AJ, Baimpas N, Salvati E, Dolbnya IP, Sui T, Ying S, et al. A state-of-the-art review of micron-scale spatially resolved residual stress analysis by FIB-DIC ring-core milling and other techniques. J Strain Anal Eng Des 2015;50:426–44, http://dx.doi.org/10.1177/0309324715596700.
[28] Lunt AJG, Korsunsky AM. Intragranular residual stress evaluation using the semi-destructive FIB-DIC ring-core drilling method. Adv Mater Res 2014;996:8–13, http://dx.doi.org/10.4028/www.scientific.net/AMR.996.8.
[29] Lunt AJG, Korsunsky AM. A review of micro-scale focused ion beam milling and digital image correlation analysis for residual stress evaluation and error estimation. Surf Coat Technol 2015;283:373–88, http://dx.doi.org/10.1016/j.surfcoat.2015.10.049.
[30] Zenotec Zr Bridge n.d. https://www.ivoclarvivadent.us/explore/zenotec-zr-bridge. [Accessed 28 May 2018].
[31] GmbH MAW. IPPS e. max Ceram n.d. http://www.ivoclarvivadent.co.uk/en/products/all-ceramics/ips-emax-technicians/ips-emax-ceram. [Accessed 28 May 2018].
[32] Jianxin D, Taichiu L. Surface integrity in electro-discharge machining, ultrasonic machining, and diamond saw cutting of ceramic composites. Ceram Int 2000;26:825–30, http://dx.doi.org/10.1016/S0272-8842(00)00024-9.
[33] Popov VL. Contact mechanics and friction: physical principles and applications. Springer; 2017.
[34] Ballard P, Constantinescu A. On the inversion of subsurface residual stresses from surface stress measurements. J Mech Phys Solids 1994;42:1767–87.
[35] Rizkalla AS, Jones DW. Mechanical properties of commercial high strength ceramic core materials. Dent Mater 2004;20:207–12, http://dx.doi.org/10.1016/S0109-5641(03)00093-9.
[36] Zahnfabrik V. VITABLOCS for CEREC. Working Instructions n.d. https://www.vita-zahnfabrik.com/en/VITABLOCS-Mark-II-25030.html. [Accessed 28 May 2018].
[37] Lunt AJ, Chater P, Korsunsky AM. On the origins of strain inhomogeneity in amorphous materials. Sci Rep 2018;8:1574 [Accessed 28 May 2018] https://www.nature.com/articles/s41598-018-19900-2.
[38] IPS. e.max Ceram Scientific Documentation n.d. http://www.roedentallab.com/downloads/emaxceramicdata.pdf.
[39] Basham M, Filik J, Wharmby MT, Chang PCY, El Kassaby B, Gerring M, et al. Data Analysis WorkbeNch (DAWN). J Synchrotron Radiat 2015;22:853–8, http://dx.doi.org/10.1107/S1600577515002283.
[40] Soper AK, Barney ER. Extracting the pair distribution function from white-beam X-ray total scattering data. J Appl Cryst 2011;44:714–26, http://dx.doi.org/10.1107/S0021889811021455.
[41] Keen DA. A comparison of various commonly used correlation functions for describing total scattering. J Appl Cryst 2001;34:172–7, http://dx.doi.org/10.1107/S0021889800019993.
[42] Proffen T, Page KL, McLain SE, Clausen B, Darling TW, TenCate JA, et al. Atomic pair distribution function analysis of materials containing crystalline and amorphous phases. Zeitschrift Für Kristallographie – Cryst Mater 2009;220:1002–8, http://dx.doi.org/10.1524/zkri.2005.220.12.1002.
[43] Dinnebier RE, Billinge SJL. Powder diffraction: theory and practice. Royal Society of Chemistry; 2008.
[44] Suryanarayana C, Norton MG. X-ray diffraction: a practical approach. Springer Science & Business Media; 2013.
[45] Mullen K, Levin I. Mitigation of errors in pair distribution function analysis of nanoparticles. J Appl Cryst 2011;44:788–97, http://dx.doi.org/10.1107/S0021889811014749.
[46] Huang PY, Kurasch S, Srivastava A, Skakalova V, Kotakoski J, Krasheninnikov AV, et al. Direct imaging of a two-dimensional silica glass on graphene. Nano Lett 2012;12:1081–6, http://dx.doi.org/10.1021/nl204423x.
[47] Ying S, Sui T, Lunt AJ, Reed RC. On the cyclic deformation and residual stress in Ni-base single crystal superalloys. Proceedings of the World Congress on Engineering 2014;2.
[48] Zhang H, Salvati E, Ying S, Lunt A, Sui T, Korsunsky AM. Effect of Pt deposition on digital image correlation analysis for residual stress measurement using FIB-DIC ringcore method. Proceedings of the World Congress on Engineering 2016;2.
[49] Eberl C. Digital Image Correlation and Tracking – File Exchange – MATLAB Central Mathworks File Exchange Server FileID – 12413 2010.
[50] Korsunsky AM, Sebastiani M, Bemporad E. Residual stress evaluation at the micrometer scale: analysis of thin coatings by FIB milling and digital image correlation. Surf Coat Technol 2010;205:2393–403, http://dx.doi.org/10.1016/j.surfcoat.2010.09.033.
[51] Song X, Yeap KB, Zhu J, Belnoue J, Sebastiani M, Bemporad E, et al. Residual stress measurement in thin films at sub-micron scale using Focused Ion Beam milling and imaging. Thin Solid Films 2012;520:2073–6, http://dx.doi.org/10.1016/j.tsf.2011.10.211.
[52] Song X, Yeap KB, Zhu J, Belnoue J, Sebastiani M, Bemporad E, et al. Residual stress measurement in thin films using the semi-destructive ring-core drilling method using Focused Ion Beam. Procedia Eng 2011;10:2190–5, http://dx.doi.org/10.1016/j.proeng.2011.04.362.
[53] Salvati E, Lunt AJ, Sui T, Korsunsky AM. An investigation of residual stress gradient effects in FIB-DIC micro-ring-core analysis. Proceedings of the International MultiConference of Engineers and Computer Scientists 2015;2.
[54] Zhang H, Senn M, Sui T, Lunt A, Brandt LR, Papadaki C, et al. On the upper and lower bounds of correlation window size in digital image correlation analysis. Proceedings of the World Congress on Engineering 2017;1.
[55] Lunt AJG, Salvati E, Ma L, Dolbyna IP, Neo TK, Korsunsky AM. Full in-plane strain tensor analysis using the microscale ring-core FIB milling and DIC approach. J Mech Phys Solids 2016;94:47–67, http://dx.doi.org/10.1016/j.jmps.2016.03.013.
[56] Mainjot AK, Schajer GS, Vanheusden AJ, Sadoun MJ. Residual stress measurement in veneering ceramic by hole-drilling. Dent Mater 2011;27:439–44, http://dx.doi.org/10.1016/j.dental.2010.12.002.
[57] Oishi M, Matsuda Y, Noguchi K, Masaki T. Evaluation of tensile strength and fracture toughness of yttria-stabilized zirconia polycrystals with fracture surface analysis. J Am Ceram Soc 2018;78:1212–6, http://dx.doi.org/10.1111/j.1151-2916.1995.tb08471.x.
[58] Imam MA, Gilmore CM. Fatigue and microstructural properties of quenched Ti- 6Al-4V. MTA 1983;14:233–40, http://dx.doi.org/10.1007/BF02651620.
[59] Lunt AJG, Kabra S, Kelleher J, Zhang SY, Neo TK, Korsunsky AM. Tensile secondary creep rate analysis of a dental veneering porcelain. Thin Solid Films 2015;596:269–76, http://dx.doi.org/10.1016/j.tsf.2015.05.039.
[60] Lunt A, Terry A, Ying S, Baimpas N, Sui T, Kabra S, et al. Characterisation of nanovoiding in dental porcelain using

small angle neutron scattering and transmission electron microscopy. Dent Mater 2017;33:486–97.
[61] Belli R, Monteiro S, Baratieri LN, Katte H, Petschelt A, Lohbauer U. A photoelastic assessment of residual stresses in zirconia-veneer crowns. J Dent Res 2012;91:316–20, http://dx.doi.org/10.1177/0022034511435100.
[62] Deville S, Chevalier J, Gremillard L. Influence of surface finish and residual stresses on the ageing sensitivity of biomedical grade zirconia. Biomaterials 2006;27:2186–92, http://dx.doi.org/10.1016/j.biomaterials.2005.11.021.
[63] Belli R, Frankenberger R, Appelt A, Schmitt J, Baratieri LN, Greil P, et al. Thermal-induced residual stresses affect the lifetime of zirconia–veneer crowns. Dent Mater 2013;29:181–90, http://dx.doi.org/10.1016/j.dental.2012.11.015.
[64] Bonfante EA, Rafferty BT, Silva NRFA, Hanan JC, Rekow ED, Thompson VP, et al. Residual thermal stress simulation in three-dimensional molar crown systems: a finite element analysis. J Prosthodont 2012;21:529–34, http://dx.doi.org/10.1111/j.1532-849X.2012.00866.x.
[65] De Jager N, de Kler M, van der Zel JM. The influence of different core material on the FEA-determined stress distribution in dental crowns. Dent Mater 2006;22:234–42, http://dx.doi.org/10.1016/j.dental.2005.04.034.
[66] Noyan IC, Cohen JB. Residual stress: measurement by diffraction and interpretation. Springer; 2013.
[67] Schajer GS. Practical residual stress measurement methods. John Wiley & Sons; 2013.
[68] Schajer GS. Measurement of non-uniform residual stresses using the hole-drilling method. Part I—stress calculation procedures. J Eng Mater Technol 1988;110:338–43, http://dx.doi.org/10.1115/1.3226059.
[69] Schajer GS, Prime MB. Residual stress solution extrapolation for the slitting method using equilibrium constraints. J Eng Mater Technol 2006;129:227–32, http://dx.doi.org/10.1115/1.2400281.
[70] Prime MB. cross-sectional mapping of residual stresses by measuring the surface contour after a cut. J Eng Mater Technol 2000;123:162–8, http://dx.doi.org/10.1115/1.1345526.
[71] Lienert U, Schulze C, Honkimäki V, Tschentscher T, Garbe S, Hignette O, et al. Focusing optics for high-energy X-ray diffraction. J Synchrotron Radiat 1998;5:226–31, http://dx.doi.org/10.1107/S0909049598001393.
[72] Withers PJ, Preuss M, Steuwer A, Pang JWL. Methods for obtaining the strain-free lattice parameter when using diffraction to determine residual stress. J Appl Cryst 2007;40:891–904, http://dx.doi.org/10.1107/S0021889807030269.
[73] Baimpas N, Lunt AJG, Dolbnya IP, Dluhos J, Korsunsky AM. Nano-scale mapping of lattice strain and orientation inside carbon core SiC fibres by synchrotron X-ray diffraction. Carbon 2014;79:85–92, http://dx.doi.org/10.1016/j.carbon.2014.07.045.